Joule

CellPress

Article

Processing Strategies for an Organic Photovoltaic Module with over 10% Efficiency

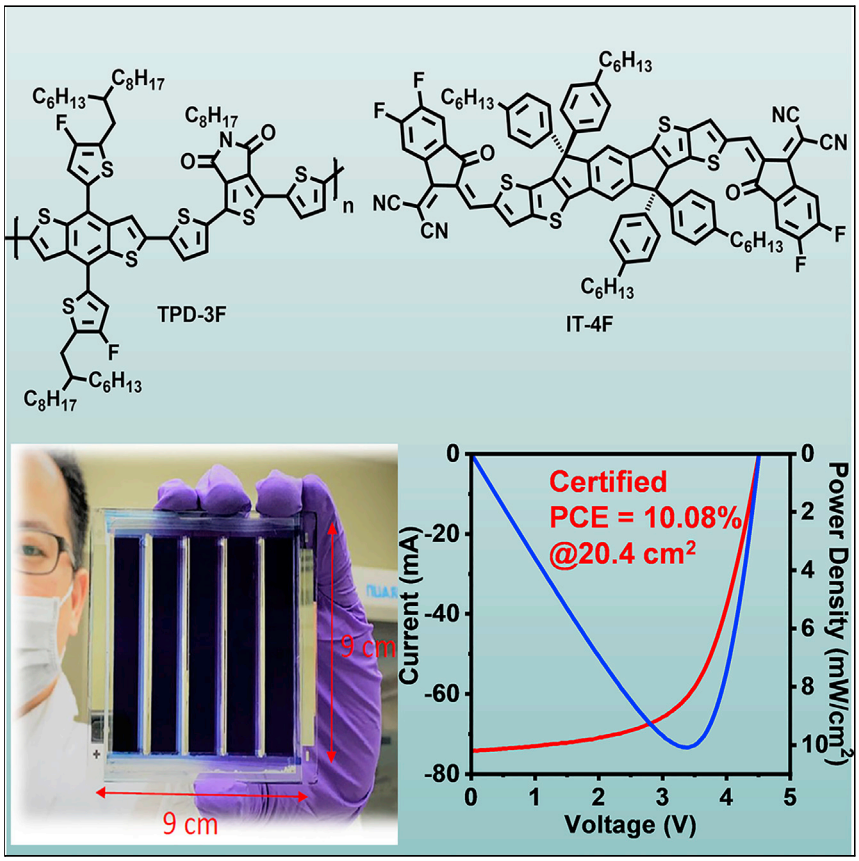

A large-area module (active area > 20 cm^2) with a power conversion efficiency (PCE) of 10.4% (certified at 10.1%) using a non-fullerene blend was demonstrated, which is by far the highest PCE reported to date. The same module also delivers a power of ~40 μW/cm^2 (PCE ~22%) under indoor lighting. Equally important, PCEs of 12%–14% were achieved for blends processed in ambient and/or without halogenated solvent.

Chuang-Yi Liao, Yao Chen, Chun-Chieh Lee, ..., Tobin J. Marks, Yi-Ming Chang, Antonio Facchetti

t-marks@northwestern.edu (T.J.M.)
ym.chang@raynergytek.com (Y.-M.C.)
a-facchetti@northwestern.edu (A.F.)

HIGHLIGHTS

A series of readily accessible polymers are utilized in organic photovoltaics

Inverted devices exhibit a high efficiency of 14% using a non-fullerene acceptor

The certified efficiency of 10.1% has been demonstrated for a module area of 20.4 cm^2

The module fabricated by blade coating exhibits a PCE of 10.40%

Liao et al., Joule 4, 189–206
January 15, 2020
https://doi.org/10.1016/j.joule.2019.11.006

Joule

CellPress

Article

Processing Strategies for an Organic Photovoltaic Module with over 10% Efficiency

Chuang-Yi Liao,[1,5] Yao Chen,[2,5] Chun-Chieh Lee,[1,5] Gang Wang,[2] Nai-Wei Teng,[1] Chia-Hao Lee,[1] Wei-Long Li,[1] Yu-Kuang Chen,[1] Chia-Hua Li,[1] Hsiuan-Lin Ho,[1] Phoebe Huei-Shuan Tan,[1] Binghao Wang,[2] Yu-Chin Huang,[3] Ryan M. Young,[2] Michael R. Wasielewski,[2] Tobin J. Marks,[2,*] Yi-Ming Chang,[1,*] and Antonio Facchetti[2,4,6,*]

SUMMARY

A series of readily accessible and scalable benzo[1,2-b:4,5-b′]dithiophene (BDT)-2,5-dithienyl-thieno[3,4-c]pyrrole-4,6-dione (TPD-T2)-based donor polymers are utilized in organic photovoltaic (OPV) cells blended with the non-fullerene acceptor IT-4F. All polymers readily dissolve in chlorine-free solvents such as xylene, and the corresponding photoactive blend films can be processed in ambient from this solvent to fabricate cells with power conversion efficiencies (PCEs) >12%–14%. Furthermore, the blend processing and OPV metrics are remarkably insensitive to the processing methodology (spin coating versus blade coating), processing solvent, polymer molecular mass and dispersity index, and the results were rationalized by UV-vis, PL, fsTA, AFM, TEM, GIWAXS, and SCLC measurements. These properties enable the first OPV modules, processed in ambient from a benign solvent, with a certified PCE of 10.1% for an area of 20.4 cm^2 and >7% after light soaking. The same module also delivers a power of ~40 μW/cm^2 (PCE ~22%) under indoor lighting.

INTRODUCTION

Bulk-heterojunction organic photovoltaic (BHJ-OPV) cells based on electron-donor + electron-acceptor photoactive blends have attracted broad research attention because organic semiconductors offer advantages vis-a-vis conventional inorganic solar materials, including mechanical flexibility, light weight, absence of toxic heavy metals, and facile module manufacture by high-throughput printing methodologies.[1–4] Importantly, achieving high-performance BHJ-OPV devices relies on materials innovation, process development, and device architecture optimization.[5–12] In particular, small OPV cells processed from halogenated solvents and various additives with single junction and tandem architectures having semiconducting non-fullerene acceptors (NFAs) have now achieved remarkable power conversion efficiencies (PCEs) of more than 16%[13] and 17%,[14] respectively, representing groundbreaking progress. These results demonstrate the significant potential of OPV-based technologies and products in the energy production and mobile power supply landscape.

Organic semiconductors not only perform very well in terms of mechanical flexibility but also exhibit excellent tunability to adjust the energy levels and film morphology

Context & Scale

Organic photovoltaic (OPV) cells have attracted broad research attention, because organic semiconductors offer advantages, including mechanical flexibility, light weight, and facile module manufacture by high-throughput printing methodologies, vis-a-vis conventional inorganic solar materials. In this study, we report the realization of new, readily accessible donor polymers and their implementation in high-efficiency solar cells and modules. These polymers yield OPV cells with certified PCEs of >14% and values of 12%–14% when the photoactive blend is processed in ambient and/or without halogenated solvents. Finally, we demonstrate the fabrication of a large active-area module (>20 cm^2) with certified PCE of 10.1% (22% indoor lighting), which is by far the highest PCE reported to date. This work represents an important step forward in the development of OPV materials for fabricating large-scale OPV modules with extremely high figures of merit, inferring that OPV cells can reach commercialization.

and enhance stability via molecular design.[10,15–20] Among the polymers widely used in OPV cells, those based on the benzo[1,2-b:4,5-b′]dithiophene moiety (BDT; Figure 1A) have shown impressive photovoltaic performance, particularly when combined with non-fullerene acceptors (NFAs).[21] For example, BDT-based wide band-gap polymers and the recently discovered NFA BTPTT-4F (IT-4F; Figure 1A) have delivered a maximum PCE of 16.4% in a single-junction OPV when processed from chloroform.[22] However, the best polymer donors reported to date require laborious multiple synthetic steps owing to their complex donor-acceptor architectures.[20,23,24] Furthermore, record OPV performance relies on using halogenated solvents, e.g., chlorobenzene and chloroform as processing solvents,[21,25,26] which are harmful to human health and the environment, and unacceptable for module manufacture. In addition, most of the high-efficency devices are reported on small photoactive areas (<1 cm^2),[9,27–29] raising the question of whether such large PCEs are conserved when the blends are implemented in large-area modules. Therefore, simplification of the polymer donor chemical structure, reduction of the cell-to-module PCE loss, and compatibility of the module fabrication procedure with industrial standards remain to be addressed. Only a few studies have investigated the challenges associated with the materials' scalability and process issues for large-area OPV manufacture and reported large-area module performance. Thus, Hong et al. (2016)[30] published PCEs up to 7.5% (certified) for a 4.15 cm^2 active-area OPV module using the poly(thieno[3,4-b]thiophene-alt-benzodithiophene) donor and $PC_{71}BM$. Zhang et al. (2018)[31] reported a remarkable PCE of 8.6% (uncertified) for an NFA-containing 3.48 cm^2 active-area OPV module with serially connected five-cell modules having a high fill factor (FF) of 65%. Finally, Mori et al. (2015)[32] reported an OPV module with PCE = 9.7% (26 cm^2; blend component chemical structure not reported), claiming scalability to even larger modules.

In this study, we report the realization of new, readily accessible donor polymers (named for simplicity TPD-n, n = 1–3, 3F; Figure 1) and their implementation in high-efficiency solar cells and modules processable from halogen-free solvents. The donor polymer backbones comprise the BDT donor moiety combined with a far simpler TPD-T2 (2,5-dithienyl-thieno[3,4-c]pyrrole-4,6-dione) acceptor moiety. The monomers were selected because of facile synthetic access and scalability as well as fine-tunability of the product polymer processability and optical absorption characteristics by simple alkyl-chain and F substitution. Specifically, the TPD unit is useful for OPV applications[33] because it affords (1) polymers with deep highest occupied molecular orbital (HOMO) levels to enhance the open-circuit voltage (V_{oc}); (2) facile introduction of diverse solubilizing alkyl chains at the *N* position; (3) when coupled with BDT, appropriate band gaps for absorption complementing typical low-band-gap NFAs. These polymers yield OPV cells with certified PCEs surpassing 14% and, equally important, values of 12%–14% when the photoactive blend is processed in ambient and/or without halogenated solvents and processing additives. Furthermore, and essential for commercialization, the OPV performance parameters are remarkably tolerant of polymer molecular mass and polydispersity variations. Finally, for the highest PCE blend, we demonstrate the fabrication of a large active-area module (>20 cm^2) with a PCE of 10.4% (after light soaking >7%) and certified at 10.1%, which is by far the highest PCE reported to date (Figure S1),[32,34] and a power of ~40 μW/cm^2 (PCE ~22%) under indoor lighting. We believe that this work represents an important step forward in the development of OPV materials for fabricating large-scale OPV modules with extremely high figures of merit, inferring that OPV cells can reach commercialization.

[1]Raynergy Tek Incorporation, 2F, 60, Park Ave. 2, Hsinchu Science Park, Hsinchu 30844, Taiwan

[2]Department of Chemistry and the Center for Light Energy Activated Redox Processes (LEAP), Northwestern University, 2145 Sheridan Road, Evanston, IL 60208, USA

[3]Department of Material Engineering, Ming Chi University of Technology, 84 Gungjuan Road, Taishan District, New Taipei City 24301, Taiwan

[4]Flexterra Incorporation, 8025 Lamon Avenue, Skokie, IL 60077, USA

[5]These authors contributed equally

[6]Lead Contact

*Correspondence: t-marks@northwestern.edu (T.J.M.), ym.chang@raynergytek.com (Y.-M.C.), a-facchetti@northwestern.edu (A.F.)

https://doi.org/10.1016/j.joule.2019.11.006

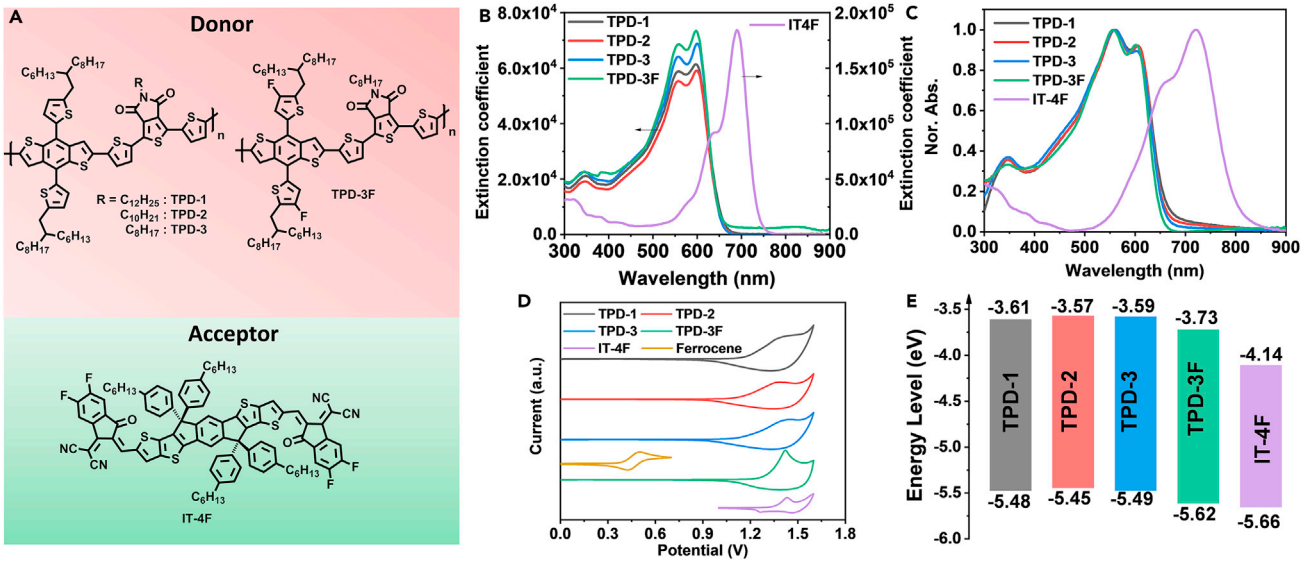

Figure 1. Blend Molecular Structures and Physical Properties

(A) Chemical structures of the TPD polymers and acceptor employed in this study.

(B and C) UV-vis absorption spectra of the polymers and IT-4F in solution (B) and in solid-state thin films (C).

(D) Cyclic voltammograms of the donors and acceptors.

(E) Energy diagrams of the polymers and IT-4F.

RESULTS AND DISCUSSION

Polymer Synthesis and Characterization

All new polymers were synthesized via Pd-catalyzed Stille coupling polycondensations using the appropriate distannylated BDT and dibrominated TPD-T2 monomers following small modifications of literature procedures (see Schemes S1 and S2 and synthetic details in the Supplemental Information).[35,36] Here, differing alkyl side chains were used primarily to adjust solubility and to optimize BHJ film morphology (*vide infra*). All polymers were purified by Soxhlet washing/extraction and obtained in overall yields of 70%–87%. Chemical purity was confirmed by ^{1}H NMR and elemental analysis. High-temperature gel permeation chromatography (GPC) analysis shows that the polymer batches used here exhibit high number average molecular masses (M_n) of 40–50 kDa and polydispersity indices (PDI) of ~2. The thermal properties of TPD polymer investigated by differential scanning calorimetry (DSC) and thermogravimetric analysis (TGA) exhibit no thermal transitions below 300°C and good thermal stabilities with decomposition temperature onsets (T_d) above 380°C (Figure S2). For the polymer affording the best PCE (TPD-3F; Figure 1A), batches with lower and higher M_n values were also synthesized to assess device performance M_n sensitivity (*vide infra*). Table 1 presents relevant chemical and physical properties of the polymers and acceptor.

The solution and thin-film photophysical properties of all polymers and IT-4F were assessed by optical absorption (ultraviolet-visible [UV-vis]) spectroscopy and cyclic voltammetry (CV) (Figures 1B–1D). The solution and solid-state polymer absorption spectra have maxima (λ_{max}) centered around 598 nm and 560 nm, respectively, with solid-state band gaps (E_g^{opt}) of 1.87–1.90 eV. These optical characteristics are complementary to those of IT-4F (λ_{max} = 590 (sol), 721 (film); E_g^{opt} = 1.55 eV), and thus, TPD-n/IT-4F blends should achieve high current densities if appropriate active layer morphologies are achieved. Note that the polymer absorption

Table 1. Properties of TPD-Based Donor Polymers and the Acceptor IT-4F

Material	M_n/PDI	Solution		Film			E_{HOMO} (eV)	E_{LUMO} (eV)
		λ_{max} (nm)	$\varepsilon \times 10^{-4}$ ($M^{-1}cm^{-1}$)[a]	λ_{max} (nm)	λ_{onset} (nm)[b]	E_g^{opt} (eV)[c]		
TPD-1	41.0/1.89	598	6.13	560	664	1.87	−5.48	−3.61
TPD-2	38.7/2.01	598	5.52	560	660	1.88	−5.45	−3.57
TPD-3	34.2/2.08	599	6.87	559	653	1.90	−5.49	−3.59
TPD-3F	51.2/2.79	598	7.33	557	653	1.90	−5.62	−3.73
IT-4F	NA	690	18.4[d]	721	801	1.55	−5.66	−4.14

[a]Extinction coefficient in chlorobenzene solution.
[b]Absorption edge of thin film.
[c]Estimated from the absorption edge of thin film.
[d]Extinction coefficient in chloroform solution.

extinction coefficients (ε) are ~5–7 × 10^{-4} $M^{-1}cm^{-1}$—somewhat lower than that of IT-4F (18.4 × 10^{-4} $M^{-1}cm^{-1}$) measured under the same conditions (Table 1). The CV plots (Figure 1) show the presence of irreversible oxidation processes located at ~1.13–1.17 eV for TPD-1, TPD-2, and TPD-3, in agreement with similar polymers,[37] whereas that of TPD-3F is shifted to higher potential (1.31 eV). No reduction peaks are observed in the investigated electrochemical window. The CV-derived HOMO levels of TPD-1, TPD-2, TPD-3, and TPD-3F measured from the onset of oxidation potentials are −5.48, −5.45, −5.48, and −5.62 eV, respectively. Thus, using different alkyl chains in the TPD-BDT polymer structure does not significantly influence the polymer HOMO energy; however, the presence of the F atom on the BDT thienyl substituents deepens the HOMO by ~0.15 eV. Therefore, TPD-3F is expected to increase the cell V_{oc}. The lowest unoccupied molecular orbital (LUMO) levels were estimated from the HOMO levels and E_g^{opt} and are −3.61, −3.57, −3.58, and −3.72 eV, respectively. These levels should be suitable for photoinduced charge separation using IT-4F with the possible exception of the TPD-3F:IT-4F blend, which has a ΔE_{HOMO} of only 0.04 eV. Thus, to understand these energetics in more detail, photoluminescence (PL) quenching experiments were carried out to quantify exciton dissociation. The comparison of the PL spectra of the pure polymer and IT-4F thin films versus those of the blends (Figure S3) indicates that both the polymer and IT-4F emissions are considerably reduced, including the TPD-3F:IT-4F blend. Thus, although definitive conclusions about charge transfer by simple PL experiments must be drawn with care,[38] we expect efficient hole and electron transfer in the OPV active layer upon photoexcitation. This result is corroborated by femtosecond transient absorption (fsTA) spectroscopy measurements for the TPD-3F-51K:IT4F blend (Figure S4). The donor was selectively excited at 700 nm as shown in Figure S4A. Energy transfer is excluded as a decay pathway because the Forster overlap is negligible. The samples were examined in a vacuum chamber without electric bias. Hole transfer was directly monitored by observing the bleach of the polymer donor ground state at 564 nm. This band does not appear in the corresponding data for the neat acceptor film excited at the same wavelength (Figure S4D). A comparison of the kinetics of the polymer bleach to the acceptor bleach (Figure S4B) shows that hole transfer occurs within the first ~300 fs following excitation, which is consistent with the strong PL quenching and high device performance (*vide infra*). The lifetime of the electron-hole pairs was monitored by the acceptor bleach at 720 nm, which decays over the next several nanoseconds. A small bleach signal lives beyond the experimental window and is assigned to a population of free carriers. Similar dynamics have been observed in other donor polymer:ITIC blends.[39]

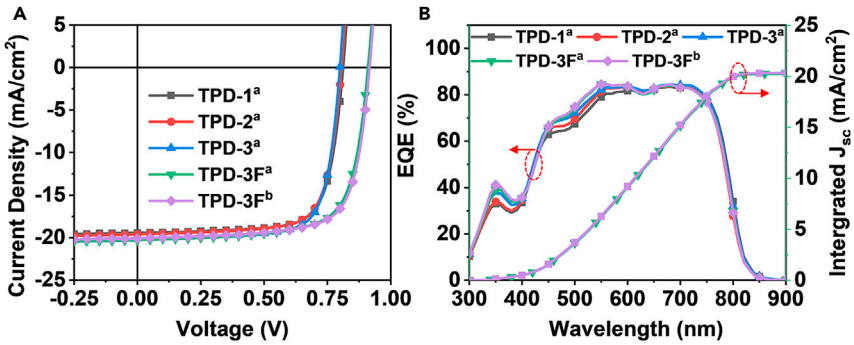

Figure 2. Cell Photovoltaic Properties

(A) Representative J-V characteristics.

(B) EQE spectra of TPD:IT-4F solar cells.

[a]Processed from *o*-xylene.

[b]Processed from chlorobenzene.

See Table 2 and Experimental Procedures for details.

Photovoltaic Properties

TPD-n-based OPV cells with inverted structures, Glass/ITO/ZnO/TPD-n:IT-4F/MoO_3/Ag, were fabricated first using *o*-xylene as the solvent, knowing that very few studies have employed halogen-free solvents for NFAs,[40] and by spin coating the blend in an N_2-filled glove box and annealing under N_2. Details are reported in the Experimental Procedures. All cells (and modules, *vide infra*) were fabricated using a polymer donor:acceptor weight ratio of 1:1 with a 0.5% weight DIO additive because this combination has been shown to generally provide the best performance in NFA-based devices.[6,7] Additional optimization of the blend performance could be achieved by further tuning these parameters. Note that the solubility of the TPD-based polymers varies little with alkyl side-chain substitution (TPD-1 and TPD-2 > 23 mg/mL, TPD-3 > 20 mg/mL in *o*-xylene at 25°C), and it is only slightly affected by fluorination (TPD-3F > 15 mg/mL). Current density-voltage (J-V) characteristics and the external quantum efficiency (EQE) spectra measured under AM 1.5 G irradiation with light intensity = 100 mW/cm^2 are shown in Figure 2, and performance metrics are summarized in Table 2.

The TPD-1 based device exhibits a V_{oc}, short-circuit current density (J_{sc}), FF, and PCE of 0.81 V, 19.4 mA/cm^2, 74.7%, and 11.7%, respectively. For the TPD-2 device featuring the TPD-based polymer with a shorter *n*-$C_{10}H_{21}$ chain, similar metrics (PCE = 11.8%) are achieved. By replacing the side-chain group with a much shorter *n*-C_8H_{17} alkyl chain in TPD-3, a slightly higher PCE of 12.1% can be achieved, mainly originating from a higher J_{sc} of 20.1 mA/cm^2 and an FF of 75.3%. Similar trends are evident from the EQE spectral results. As expected, the TPD-3F devices yield a significantly higher V_{oc} than those of the other TPDs, significantly increasing PCE from ~12% to 13.8% (Table 2). The highest-performing device achieves a V_{oc} and J_{sc} of 0.91 V and 20.5 mA/cm^2, respectively. The calculated J_{sc} by integration from EQE data is 20.3 mA/cm^2, which is consistent with the J-V measurements. Importantly, statistically identical performance (V_{oc} = 0.92 V, J_{sc} = 20.1 mA/cm^2, FF = 73.0%, PCE = 13.5%) can be achieved by processing the TPD-3F:IT-4F blend with chlorobenzene (Figure 2). Finally, TPD-3F:IT-4F cells were fabricated using *o*-xylene with an anti-reflection coating, affording a V_{oc} = 0.92 V, J_{sc} = 21.6 mA/cm^{-2}, FF = 72.3%, and PCE = 14.4%, which was certified at PCE = 14.2% (Figure S5).

Table 2. Summary of Photovoltaic Parameters for the Indicated TPD-n:IT-4F MoO3-Based Devices[a]

Entry	Blend	V_{oc} (V)	J_{sc} (mA/cm^2)	FF (%)	PCE_{Max} (%)	PCE_{Ave} (%)
1	TPD-1:IT-4F[b]	0.81	19.4	74.7	11.7	11.2
2	TPD-2:IT-4F[b]	0.81	19.6	74.2	11.8	11.5
3	TPD-3:IT-4F[b]	0.80	20.1	75.3	12.1	11.9
4	TPD-3F:IT-4F[b]	0.91	20.5	73.8	13.8	13.6
5	TPD-3F:IT-4F[c]	0.92	20.1	73.0	13.5	13.4
6	TPD-3F:IT-4F[b,d]	0.92	21.6	72.3	14.4	–
7	TPD-3F:IT-4F[b,d,e]	0.93	21.1	72.6	14.2	–

[a]Device parameter standard deviation <5%, from a minimum of 10 devices.
[b]Blend processed from *o*-xylene.
[c]Blend processed from chlorobenzene.
[d]With anti-reflection coating.
[e]Certified device of entry 6. Film thickness ~100–110 nm. Donor:acceptor weight ratio = 1:1 with 0.5% DIO additive (see Experimental Procedures for details).

Molecular Weight and Blend Processing Ambient Tolerance

Conjugated polymers are widely used as electron donors in OPV blends because of their unique morphological properties enabling the formation of optimized interpenetrating networks with small-molecule electron acceptors. Despite these attractions, the sensitivity of BHJ film morphology and OPV performance parameters to the polymer donor molecular mass and PDI can substantially limit the scalability/cost of the synthesis, fidelity/process window for device fabrication, and module mass production.[41] To evaluate this aspect quantitatively, three different TPD-3F batches with M_n varying from 34 K to 64 K were synthesized by modifying the reaction conditions (see Table 3 and Supplemental Information for details). TPD-3F:IT-4F devices based on these donor batches were fabricated, and the device performance at AM 1.5G 100 mW/cm^2 light is summarized in Table 3. Compared with the medium M_n polymer batch (51.2 kDa/2.79) investigated above, which in this group of control devices afford a PCE/PCE_{max} of 13.4/13.8% (V_{oc} = 0.91 V, J_{sc} = 21.0 mA/cm^2, FF = 72.3%), the high- (63.8 kDa/2.49) and low-M_n (34.5 kDa/4.27)-based blends afford statistically indistinguishable PCE/PCE_{max} of 13.2/13.8% (V_{oc} = 0.92 V, J_{sc} = 19.8 mA/cm^2, FF = 75.6%) and 13.2/13.5% (V_{oc} = 0.91 V, J_{sc} = 20.2 mA/cm^2, FF = 73.4%), respectively. These results indicate that these TPD-BDT polymers are not only easily synthesized but afford OPV performance that is remarkably tolerant to the processing solvent, diverse polymer substituents, and M_ns. It will be seen that these performance trends are in good agreement with the blend morphological and charge transport trends (*vide infra*).

TPD-3F:IT-4F Film Morphological and Charge Transport Characterization

To understand the excellent OPV performance parameters and, equally important, their minimal sensitivity to the chemical structure and M_n, BHJ film morphological and charge transport characteristics were assessed by atomic force microscopy (AFM), transmission electron microscopy (TEM), two-dimensional (2D) grazing-incidence wide-angle X-ray scattering (GIWAXS), and charge-selective space-charge-limited current (SCLC) measurements. AFM images of the pristine films and of the corresponding blends (Figure S6 and Figure 3A inset, respectively) indicate similar film morphologies characterized by smooth surfaces with RMS (σ_{RMS}) values of 0.6–0.7 nm and 0.9–1.3 nm, respectively. The images also show that for all blends the BHJ constituents aggregate into interpenetrating networks, and such nanoscale phase separation is a pre-requisite for excellent device performance. These results,

Table 3. Summary of Photovoltaic Parameters for TPD-3F:IT-4F[a] Devices Fabricated with Polymers with Different Molecular Weights[a,b]

Polymer Sample	Mn (kDa)	Mw (kDa)	PDI	V_{oc} (V)	J_{sc} (mA/cm^2)	FF (%)	PCE_{Max} (%)	PCE_{Ave} (%)
High	63.8	159.0	2.49	0.92	19.8	75.6	13.8	13.2
Medium	51.2	143.1	2.79	0.91	21.0	72.3	13.8	13.4
Low	34.5	147.2	4.27	0.91	20.2	73.4	13.5	13.2

[a]Device parameter standard deviation < 5%, from minimum of 10 devices.
[b]Blend processed from *o*-xylene. Film thickness ~100 nm without antireflection coating.

further corroborated by the almost identical TEM images (Figure S7), are consistent with the insensitivity of the device performance with the TPD-3F polymer M_ns.

SCLC measurements were made on hole-injection-only and electron-injection-only diodes of structure ITO/MoO_3/TPD-3F:IT-4F/MoO_3/Al and ITO/ZnO/TPD-3F:IT-4F/LiF/Al, respectively (Figure S8). The hole mobilities (μ_h; Tables S1 and S2) of the pristine polymer films demonstrate substantial and similar hole transport capacities (μ_h = 1.51 × 10^{-3} cm^2/Vs [TPD-1], 2.24 × 10^{-3} cm^2/Vs [TPD-2], 1.88 × 10^{-3} cm^2/Vs [TPD-3], 1.68 × 10^{-3} cm^2/Vs [TPD-3F-34K], 2.41 × 10^{-3} cm^2/Vs [TPD-3F-51K], 1.24 × 10^{-3} cm^2/Vs [TPD-3F-64K]). For blend films, the μ_hs remain high and in a narrow range (9.03 × 10^{-4} cm^2/Vs [TPD-1], 8.47 × 10^{-4} cm^2/Vs [TPD-2], 8.25 × 10^{-4} cm^2/Vs [TPD-3], 8.63 × 10^{-4} cm^2/Vs [TPD-3F-34K], 8.13 × 10^{-4} cm^2/Vs [TPD-3F-51K], 8.17 × 10^{-4} cm^2/Vs [TPD-3F-64K]) while the electron mobilities are somewhat lower(μ_e ~3 × 10^{-4} cm^2/Vs) but again, independent of blend chemical composition and M_n. Overall, the SCLC results indicate that all BHJ blends exhibit similar and sufficiently balanced charge transport capacities to provide good FFs and J_{sc}s (Table 2), and considering the limited μ_e values, further performance enhancement is expected by using a more suitable acceptor.

Further analysis of the polymer and blend film morphologies was carried out by GIWAXS experiments. The GIWAXS patterns and the corresponding line cuts for the blend films are provided in Figures 3 and S9, and data are summarized in Tables S3–S7. As shown in the Figure S9, all neat polymer thin films exhibit a preferential π-face-on orientation of the polymer chains with respect to the substrate surface. From the in-plane (100) reflection (q_{xy}), it is found that when the alkyl chain length decreases from TPD-1 to TPD-3, the lamellar d-spacing (d_l) contracts from 27.71 Å (TPD-1), to 26.83 Å (TPD-2) to 25.87 Å (TPD-3), whereas the correlation length increases slightly from 92.63 Å to 98.51 Å. Similarly, for the out-of-plane (010) reflections, the π-π intermolecular d-spacing distance (d_π) contracts from 3.62 Å to 3.59 Å, with the peak intensity exhibiting the same trend. Upon fluorination of the BDT unit in TPD-3F, a small d_l increase is observed, which is only slightly sensitive to the polymer M_n (d_l = 26.17 Å for TPD-3F-34K and TPD-3F-64K, and 26.37 Å for TPD-3F-51K). However, the corresponding correlation length for the TPD-3F-64K samples (99.32 Å) is larger than that of the lower M_n materials (83.11 Å for TPD-3F-34K and 85.76 Å for TPD-3F-51K), suggesting that a higher molecular weight enhances texturing of the alkyl-chain periodicity. However, all the TPD-3F donor polymer batches exhibit an almost identical d_π of 3.63 Å, again with the largest stacking peak intensity observed for TPD-3F-64K, suggesting that the greater M_n induces the most ordered texture for π-π stacking as well. Note, owing to the broad and weak peak distributions, we cannot extract the accurate correlation lengths for the (010) direction. Crystallization and degree of texturing in conjugated polymer films are affected by several parameters including the molecular structure, processing conditions, thermal history, M_n, as well as polydispersity index.[42–44] Although the effect of the M_n variation on degree of crystallinity varies, increased PDI typically

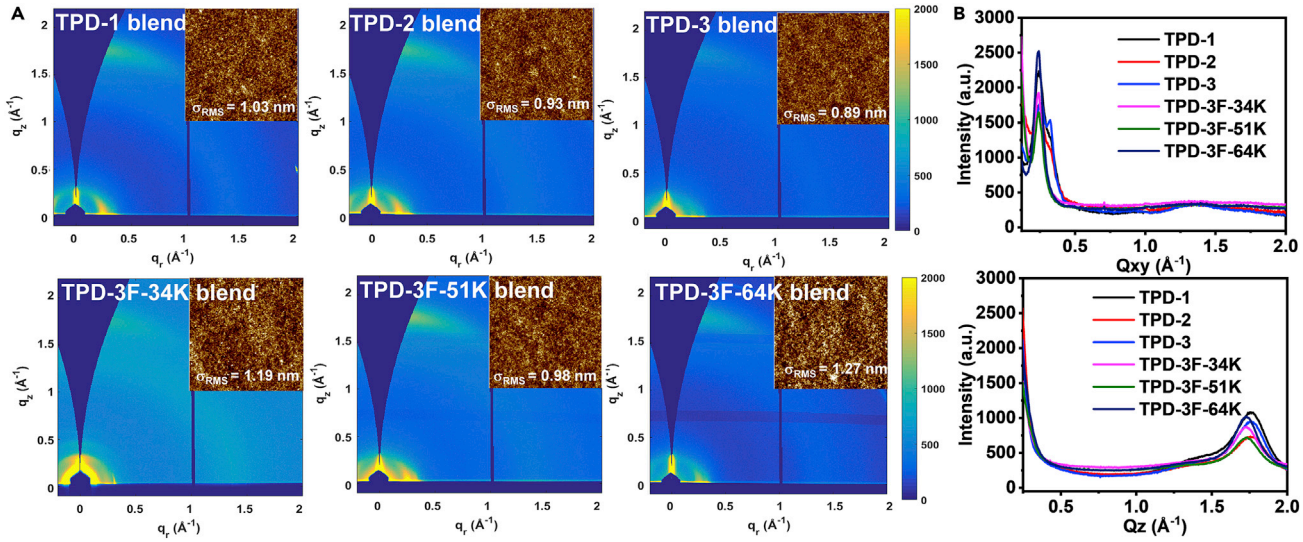

Figure 3. Thin-Film Morphology and Microstructure

(A) Two-dimensional (2D) GIWAXS AFM phase images (insets, 5 × 5 μm) of the indicated blend films.

(B) Corresponding in-plane and out-of-plane line cuts.

suppresses crystallization. Thus, for our TPD-3F series, enhanced film texturing going from the TPD-3F-34K to the TPD-3F-64K samples may also originate from the progressive reduction of the PDI from 4.27 (TPD-3F-34K) to 2.79 (TPD-3F-51K) to 2.49 (TPD-3F-64K).[45] Finally, although not clearly visible in the neat acceptor 2D-GIWAXS images, from the corresponding in-plane line-cut profiles, very weak reflections are located at 0.38 $Å^{-1}$ and 1.46 $Å^{-1}$, which can be assigned to the (100) alkyl-chain and (010) π-π intermolecular periodicities, respectively.

The GIWAXS data for the blend films indicate similar preferential face-on π-π intermolecular stacking distributions of the donor polymer chains with respect to the substrate surface (Figure 3). For the TPD-1:IT-4F, TPD-2:IT-4F, and TPD-3:IT-4F blends, the reflections located at q_{xy} = 0.24–0.25 $Å^{-1}$ are attributed to the donor polymer (100) alkyl-chain stacking, whereas the peaks located at q_{xy} = 0.31–0.33 $Å^{-1}$ can be attributed to the IT-4F (100) alkyl-chain periodicity. Similar crystallization of an NFA phase in a blend was observed recently.[46] On decreasing the donor alkyl-chain length (TPD-1 → TPD-3) in the blend, the d_l of the donor polymer contracts from 26.30 to 25.15 $Å^{-1}$, whereas the correlation length monotonically increases from 75.76 (TPD-1), 112.37 (TPD-2), to 119.23 Å (TPD-3). For the TPD-1:IT-4F and TPD-2:IT-4F films, only weak peaks from the IT-4F alkyl-chain periodicity can be observed; however, this reflection becomes much stronger and sharper for the TPD-3:IT-4F blend, corresponding to a significant correlation length of 171.45 Å. For the out-of-plane stacking, an identical reflection at q_z = 1.76–1.77 $Å^{-1}$ corresponds to an almost identical d_π of 3.56–3.57 Å. However, the π-π stacking intensity gradually falls from TPD-1:IT-4F to TPD-3:IT-4F, suggesting suppressed intermolecular ordered stacking with the contraction of the polymer alkyl chains. The relatively weak reflection with a similar diffraction intensity at q_z = 1.48–1.56 $Å^{-1}$ is attributed to the IT-4F (010) π-π intermolecular stacking with a periodicity d_π of 4.03–4.26 Å, larger than the minimum π-π distances in IT-4F single crystals (3.2–3.4 Å).[47] For the TPD-3F:IT-4F blend films with donor polymers of different M_n, the peaks located at q_{xy} = 0.25 $Å^{-1}$ can be attributed to the donor polymer (100) alkyl-chain periodicity, whereas those located at q_{xy} = 0.31–0.32 $Å^{-1}$ can be attributed to the IT-4F (100)

alkyl-chain periodicity, similar to that observed for the TPD-3:IT-4F blend films. Thus, upon increasing the donor M_n, d_l remains pinned at 25.10 Å (similar to the TPD-3:IT-4F blend); however, the medium M_n TPD-3F-51K blend exhibits a slightly larger correlation length: 92.13 Å for TPD-3F-34K:IT-4F, 104.48 Å for TPD-3F-51K:IT-4F, and 93.91 Å for TPD-3F-64K:IT-4F. The out-of-plane reflections located at q_z = 1.76–1.77 $Å^{-1}$ can be attributed to donor polymer (010) π-π stacking at a similar d_π of 3.56–3.57 Å, with the largest M_n polymer exhibiting the strongest reflection. In addition, the out-of-plane alkyl-chain periodicity peaks for both donor polymer and IT-4F are only observed for the TPD-3F-34K:IT-4F blend samples, suggesting the existence of out-of-plane alkyl-chain ordered texture. Overall, the GIWAXS results indicate that within this polymer family (1) elongation of alkyl chain dimension increases the interlamellar distance as expected; (2) variation in alkyl chain size, fluorination, and molecular mass minimally affect the pristine polymer and BHJ texturing and the π-π intermolecular periodicity; and (3) the IT-4F acceptor crystallizes more readily in the blend films, especially with the fluorinated donor polymer. Thus, these results, combined with the morphological and charge transport data, show that the major TPD-3F-based blend performance enhancement originates primarily from the electronic structure differences of this polymer (especially the lower HOMO) versus that of the fluorine-free analogs.

BHJ Processing: Module Fabrication and Stability

Before module assembly and evaluation using the optimized and best-performing TPD-3F-51K:IT-4F BHJ blend, we address an important issue directly affecting module production. It is generally accepted that most non-fullerene OPV devices must be encapsulated under more or less stringent inert atmosphere conditions for long-term stability.[2] However, for practical large-scale manufacture, it is important that BHJ films be processed under ambient. For these reasons, we evaluated TPD-3F:IT-4F cells for which all BHJ film coating and baking steps were carried out under N_2 versus those in which the entire process was carried out under air (details in the Experimental Procedures). Figure 4A plots the device performance parameters of the TPD-3F:IT-4F devices fabricated in the different atmospheres. Thus, devices entirely processed in an N_2-filled glove box perform optimally with V_{oc} = 0.90 V, J_{sc} = 20.9 mA/cm^2, FF = 69.4%, and PCE_{max} = 13.1%, whereas all steps in ambient except annealing under N_2, and those fully fabricated in ambient, continue to exhibit respectable PCEs of ~12%. The slight performance degradation results from an eroded FF (from ~70% to ~64%) because both V_{oc} and J_{sc} remain essentially pinned at 0.9 V and ~21 mA/cm^2, respectively. Importantly, this result demonstrates that TPD-3F and the corresponding BHJ blend can withstand the ambient O_2 and moisture exposure essential for large-scale OPV module manufacture and industrialization. Furthermore, because blade coating is commonly used for OPV fabrication, TPD-3F:IT-4F cells were also fabricated in ambient using this coating technique (see Figure 4A and Experimental Procedures for device fabrication details). As shown in the Figure S10 and Table S8, the TPD-3F-51K:IT-4F solar cells fabricated by blade coating show negligible PCE loss versus spin-coated ones (13.4% versus 13.8%). Furthermore, the blade-coated devices have good film-thickness uniformity, and a PCE of 12.8% is also achieved with a blend thickness of 183 nm. These results demonstrate that TPD-3F:IT-4F is an excellent candidate for large-area device manufacture.

Next, OPV modules were fabricated using *o*-xylene as the processing solvent first by spin coating the blend in ambient. Figures 4B and 4C show images of a representative module consisting of a five (stripe) sub-cells monolithically integrated and connected in series by ITO-to-Ag interconnects. Figure 4D shows the I-V curves of the spin-coated module measured under AM 1.5 G solar irradiation at an intensity

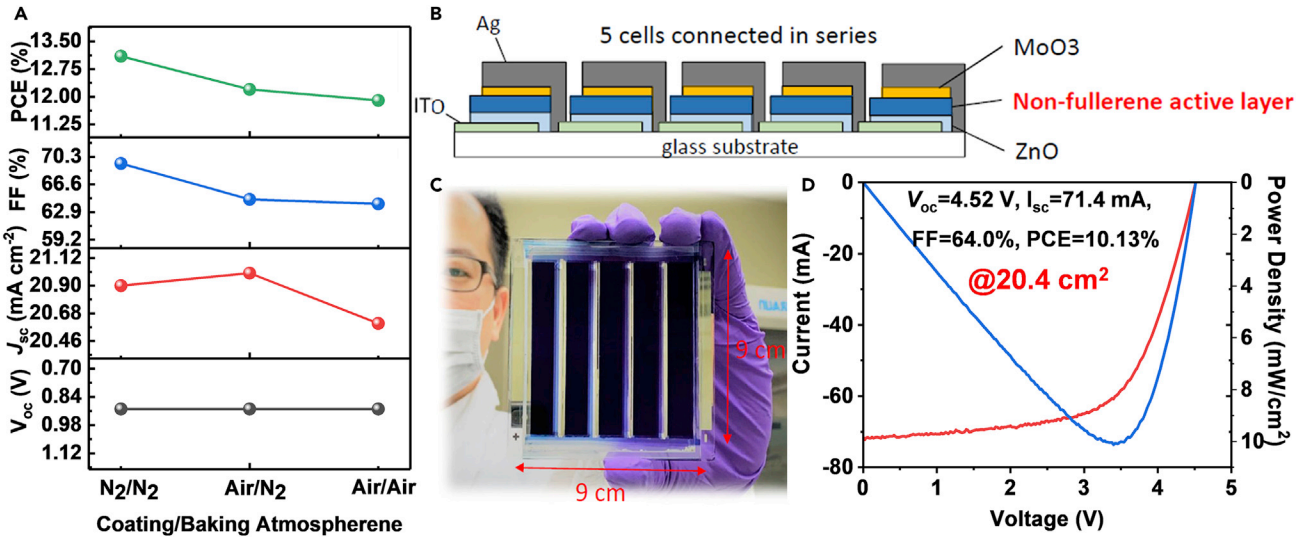

Figure 4. Cell and Module Photovoltaic Properties

(A) Photovoltaic parameters of TPD-3F-51K:IT-4F MoO_3-based devices fabricated in different atmospheres and measured under AM 1.5 G solar irradiation at an intensity of 100 mW/cm^2.

(B) Schematic of the TPD-3F-based OPV module structure.

(C) The real photograph of TPD-3F-based OPV module.

(D) *I-V* characteristics of the TPD-3F-based OPV module (module area = 20.4 cm^2) measured under AM 1.5 G solar irradiation at an intensity of 100 mW/cm^2.

of 100 mW/cm^2, which provides a PCE_{max} of 10.13% with a V_{oc} of 4.52V, I_{sc} of 71.4 mA, and FF of 64.0%, affording a maximum power density of 10.13 mW/cm^2. It must be noted that the geometric FF (effective area/total area) on a 9 cm by 9 cm substrate is ~37% (29.75 cm^2/81 cm^2), and the effective area was defined by the overlapping area of the cathode and the anode in the module (5.95 cm^2 per cell, 5 cells in series). For real module manufacturing, the geometric FF could be increased by using a more precise equipment or adopting a laser patterning technology. Here, to ensure accuracy of the PCE calculation, an additional aperture mask was attached during sample illumination, defining the active area as 20.4 cm^2 (4.08 cm^2 per cell). This module was also evaluated by the Newport PV Lab, yielding a certified PCE of 10.08% under quasi-steady-state conditions, which is a stabilized performance under continuous irradiation (Figure S11). The spectral mismatch was 0.99, and the module was certified with V_{oc} = 4.52 V, I_{sc} = 74.1 mA, and FF = 61.4%. Compared with the PCEs achieved for the small cells (0.04 cm^2, ~13% PCE), the present large module exhibits only a ~20% cell-to-module loss. To the best of our knowledge, this certified module PCE is the highest value reported to date for solution-processed blends.[32,34] Equally important, the module fabricated by blade coating the blend instead of spin coating exhibits statistically identical performance (PCE = 10.40%, V_{oc} = 4.45 V, I_{sc} = 78.7 mA, FF = 60.5%; Figure S12). Furthermore, we began addressing the replacement of the difficultly implemented MoO_3 with a more scalable HTL interlayer such as commonly used PEDOT:PSS (CLEVIOS HTL Solar).[48] Details and discussion are reported in Experimental Procedures and in the Supplemental Information (Table S9). Briefly, the control cell of structure glass/ITO/ZnO/TPD-3F:IT-4F/PEDOT:PSS/Ag exhibits poor performance (J_{sc} = 16.8 mA/cm^2, FF = 57.4%, V_{oc} = 0.61 V, PCE = 5.88%) likely originating from the energy-level mismatch between the HTL (−5.0 eV) and the donor polymer (−5.62 eV, see energy diagram in Figure S13). By using a modified PEDOT:PSS (m-PEDOT:PSS), which exhibits a deeper work function of −5.2 eV, the resulting cell (glass/ITO/ZnO/TPD-3F:IT-4F/m-PEDOT:PSS/Ag) performs significantly better with a V_{oc} of 0.89 V, J_{sc} of

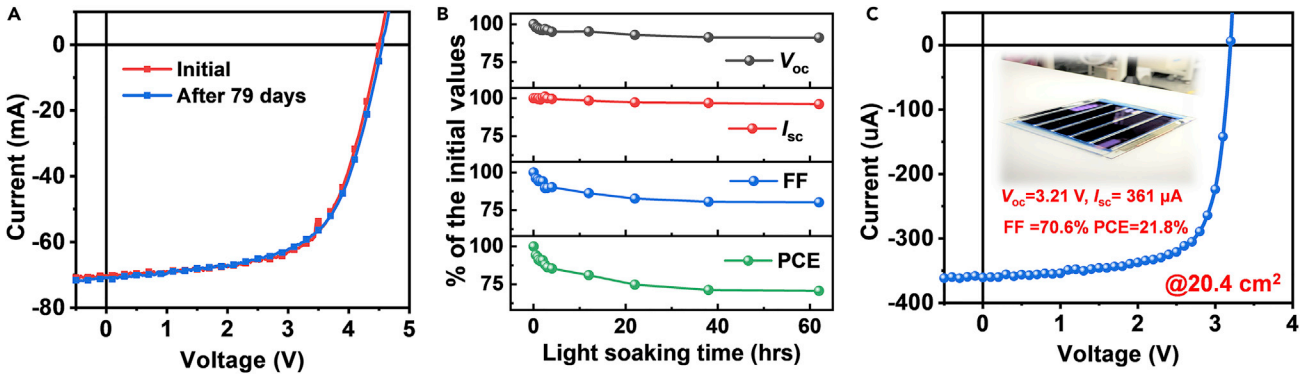

Figure 5. Module Stability and Indoor Photovoltaic Response

(A) Module stability test in dark (initial PCE = 9.89%).

(B) Module stability test under light-soaking (initial PCE = 9.84%).

(C) Representative J-V characteristics of TPD-3F-51K:IT-4F module under a fluorescent lamp with a luminance of 1,000 lux.

17.7 mA/cm^2, FF of 67.3%, and PCE of 10.6%. The corresponding blade-coated m-PEDOT:PSS-based module (Figure S13C) affords a respectable PCE of 6.77% considering that all layers, except the contacts, are blade coated. Further optimization should be achievable by further lowering the solution-processed HTL work function and reducing the leakage current by improving the HTL morphology.[48]

Device stability is another important factor for commercialization. Thus, the MoO_3-based module and the control-cell stability were tested both under dark and light-soaking conditions. As shown in Figure 5A, the module (and the cell, not shown) retains >98% of the original PCE (9.9% → 9.7%) after ~80 days storage under ambient (T = 21°C–25°C) in the dark, suggesting good blend morphological and chemical stability. Light-soaking stability tests for the module and the cell are summarized in Figures 5B and S14. The devices were first measured under standard AM 1.5 G solar conditions (100 mW/cm^2), and this module exhibits an initial PCE of ~9.84% (FF ~62.1%; V_{oc} ~4.54 V; I_{sc} ~71.2 mA), whereas that of the cell is 13.1% (FF ~69.8%; V_{oc} ~0.91 V; J_{sc} ~20.6 mA/cm^2). Subsequently, the light-soaking test was conducted under a metal halide lamp with an intensity of 100 mW/cm^2 at 55°C for ~62 h. The results indicate that both devices exhibit typical burn-in behavior[11] with erosion of both J_{sc} and V_{oc} and a larger decrease in the FF after ~ 20-h light soaking, after which the PCE stabilizes to ~70% (module) and ~85% (cell) of the initial value. The combined data indicate that this blend can exhibit stable characteristics after initial loss, with the module retaining a respectable PCE of ~7.1%, which is promising for achieving commercial entry. Note that enhanced robustness can be ensured by more efficient encapsulation of the module.

Additionally, note that traditional solar cells are used primarily for outdoor applications. However, devices powered by indoor light have become attractive owing to the rapid market growth of low-power-consumption electronics and their self-sustainable operation. The best (MoO_3-based) cell and module were tested with a fluorescent lamp (1,000 lux TL84 fluorescent, see Figure S15 for details of the light emission spectrum). As shown in Figures 5C and S16, the power generation of the cell and module reach 48.5μW/cm^2 and 40.2 μW/cm^2, respectively, which are equal to PCEs of 26.2% (V_{oc} = 0.75 V, I_{sc} = 3.98 μA, and FF = 65.1%) and 21.8% (V_{oc} = 3.21 V, I_{sc} = 361 μA, and FF = 70.6%), respectively, based on a light power of 185 μW/cm^2 at 1,000 lux TL84 fluorescent. For the module, this power generation is sufficient to

power electronics such as the RFID tags, wrist watch calculators, and quartz oscillators.[49]

Conclusions

We have synthesized and characterized a new series of TPD donor polymers and investigated alkyl chain length and fluorination effects on their BHJ-OPV performance with the small-molecule non-fullerene acceptor IT-4F. All TPD polymers exhibit good solubilities in organic solvents, adequate hole transport capacity, and matched energy levels with IT-F4. Solar cells based on the TPD: IT-4F blends exhibit maximum certified PCE of >14% as well as ~12% when fabricated in air and using a chlorine-free solvent. The TPD:IT-4F cell performance exhibits excellent tolerence to variations to polymer molecular mass, polydispersity, fabrication environment (ambient or N_2), and film deposition technique (spin coating or blade coating). Importantly, a certified PCE of >10% is demonstrated for a module fabricated under ambient with an area of 20.4 cm^2, which, to our knowledge, is the largest value reported to date for a solution-processed solar cell module. Additionally, these modules exhibit a power generation of ~40 $\mu W/cm^2$ under indoor lighting conditions. Dark and light-soaking stability tests demonstrate that after initial loss, the PCE of the module stabilizes to ~70% of the initial performance, thus ~7%, which remains among the largest to date when compared with certified, but not light-soaked, modules (Figure S1), and it is a respectable metric for commercial module introduction. We believe that this work represents an important step in the development of materials for fabricating and manufacturing large-scale OPV modules with extremely high figures of merit, inferring that OPV cells can reach commercialization.

EXPERIMENTAL PROCEDURES

Materials

All chemicals, unless otherwise specified, were purchased from commercial resources and used as received. Tetrahydrofuran (THF) and *o*-xylene were passed through molecular sieves before use, and other solvents and reagents were purchased from commercial sources and used without additional purification. The polymer building blocks M1, M2, M3, and D1 were synthesized according to the literature.[35,36] The electron acceptor, IT-4F, was synthesized by modifying a previously reported procedure.[50]

Polymer Synthesis and Characterization

Details of polymer synthesis are reported in the Supplemental Information. ^1H and ^{13}C NMR spectra were measured using a Bruker Avance 500 MHz spectrometer. Variable-temperature NMR spectra were recorded on a Varian Unity Inova 500 MHz spectrometer. Chemical shifts for ^1H and ^{13}C spectra are referenced to residual protio-solvent signals (δ ^1H = 7.24 ppm for $CDCl_3$; δ ^{13}C = 77 ppm for $CDCl_3$; δ ^1H = 6.0 ppm for $C_2D_2Cl_4$). UV-vis absorption and PL spectra were measured by using Hitachi U-3900 and F-7000 spectrometers. CV was conducted on a CH Instruments electrochemical analyzer. Glassy carbon was used as the working electrode with an Ag/AgCl electrode as the reference electrode, whereas 0.1 M tetrabutylammonium hexafluorophosphate in dry acetonitrile was the electrolyte. CV curves were calibrated using ferrocene as the internal standard, with the HOMO set at −4.7 eV with respect to zero vacuum level. The HOMO energy levels were obtained from the equation HOMO = $-(E_{ox}^{onset} - E_{(ferrocene)}^{onset} + 4.7)$ eV. The LUMO levels were obtained from the relationship LUMO = (E_g + HOMO) eV. DSC measurements were performed on an Mettler Toledo DSC822e with a heating/cooling rate of 10°C per min. TGA scans were recorded on the TA-600 instrument with a heating rate of 10°C/min. Polymer molecular masses were determined on a Polymer

Laboratories PL-GPC 220 instrument equipped using 1,2,4-trichlorobenzene (stabilized with 125 ppm of BHT) as eluent at 150°C and calibrated to polystyrene standards. The TPD polymers were pre-dissolved in 1,2,4-trichlorobenzene with a concentration of ~1.00 mg/mL while shaking for 2 h at 150°C.

Film Characterization

The thin-film morphologies were analyzed by AFM in tapping mode under ambient conditions (Dimension Icon Fast Scan probe microscope). GIWAXS measurements were performed at the Advanced Photon Source at Argonne National Laboratory. Film samples were prepared on the same glass/ITO/ZnO substrates as used for processing solar cells. The samples were irradiated at incidence angles from 0.130° to 0.140° in vacuum at 10.915 keV for two summed exposures of 2.5 s each.

Transient Absorption Spectroscopy Measurements

Transient absorption experiments for thin films were performed as described previously.[51] Briefly, ~40% of the output of a 1 kHz amplified Ti:sapphire system at 827 nm (1 W, 100 fs, Spitfire, Spectra Physics) is used to pump a laboratory-constructed optical parametric amplifier that is then tuned to the specific excitation wavelength. The pump is depolarized to minimize polarization-specific dynamics. The pump spot size was set to 0.5 mm diameter (1/*e*), and the pulse energy is attenuated to be ~200 nJ/pulse to minimize singlet-singlet annihilation. The probe in the fsTA experiment is generated using 10% of the remaining output by driving continuum generation in a sapphire plate (430–850 nm) or a proprietary crystal from Ultrafast Systems (850–1,600 nm). Pump and probe are spatially and temporally overlapped at the sample. The transmitted probe is detected on a commercial spectrometer (customized Helios-EOS, Ultrafast Systems, LLC).

Prior to kinetic analysis, the fsTA data are background- and scatter-subtracted and chirp-corrected, and the visible and NIR datasets are spectrally merged (Surface Xplorer 4, Ultrafast Systems, LLC). Single-wavelength kinetic analysis is performed in Origin 2019 by fitting the time-dependent signals $S(t)$ to the convolution of Gaussian instrument response with temporal width w and (1) a multi-exponential decay with amplitudes a_i and time constants τ_i, (2) a delta function with amplitude a_0, centered at the zero of pump-probe delay (t_0) to account for instrument-limited coherence artifacts, and (3) offsets for before (S_0) and after (S_0') t_0 to account for any signals present beyond the experimental window:

$$S(t) = e^{-t^2/w^2} * \begin{cases} S_0 & t<t_0 \\ S_0' + a_0\delta(t-t_0) + \sum_{i=1}^{N} a_i \exp[-(t-t_0)]/\tau_i & t \geq t_0 \end{cases}. \quad \text{(Equation 1)}$$

The time-resolution is given as $2w\sqrt{\ln 2}$ = 300 fs (full width at half maximum, FWHM).

OPV Cell Fabrication and Characterization

All cells were fabricated using a blend solution prepared by mixing the donor polymer (9 mg/mL) with IT-4F (9 mg/mL) in 1 mL of solvent (*o*-xylene or CB) and with the addition of 0.5% weight (versus solvent) of DIO. The solutions were stirred at 120°C for a minimum of 4 h. The solutions were cooled down to room temperature (~10 min after removing from hot plate) with continued stirring before thin-film deposition.

(1) Cells fabricated by spin coating under N_2: OPV cells of structure ITO/ZnO/TPD-x:IT-4F/MoO_3/Ag were fabricated by spin coating the ZnO precursor

solution (consisting of 0.3 M zinc acetate dihydrate and 0.3 M ethanolamine in 2-propanol) on top of pre-cleaned ITO glass substrates followed by annealing at 120°C for 15 min in air. Subsequently, the samples were transferred into an N_2-filled glove box, and the blend was spin coated on top of the ZnO layer to form a ~100-nm-thick BHJ layer. Next, the samples were annealed at 120°C in a glove box for 5 min and then transferred to an evaporator. Finally, 8-nm-thick MoO_3 and a 100-nm-thick Ag electrode were deposited by thermal evaporation at a pressure of approximately 10^{-6} Torr. The active area of the device was defined by a shadow mask and an additional aperture mask. Finally, the devices were encapsulated in N_2-filled glove box by cavity glass with a UV-curable sealant (SAES, ZeoGlue-G). A bead of sealant was applied around the edge of the cavity glass. Then the cavity glass was placed onto the module and pressed down firmly to thin the sealant, and the sealant cured with a 400 W metal halide lamp for 20 s.

(2) Cells fabricated by spin coating in air and annealing under nitrogen: device fabrication is as described in (1) except that the active layer deposition was carried out in air at an ambient temperature of 21°C and relative humidity of 45%. The devices were then transferred into an N_2-filled glove for annealing.

(3) Cells fabricated by spin coating and annealing in air: device fabrication was as described in (1) with the exception of the deposition and annealing of the active layer being processed in air with an ambient temperature of 21°C and relative humidity of 45%. Then the devices were transferred into an evaporator for MoO_3/Ag deposition.

(4) Cells fabricated by blade coating in air: device fabrication is as described in (1) except that the active layers were deposited by blade coating and processed in air with an ambient temperature of 21°C and relative humidity of 45%. After the film deposition, the devices were transferred into an N_2-filled glove box, and films were annealed as in (2).

(5) Cells incorporating normal and modified PEDOT:PSS as the HTL: device fabrication is as described in (1) except that the HTL was prepared by spin coating a PEDOT:PSS solution (normal PEDOT:PSS from CLEVIOS HTL Solar or modified EDOT:PSS from RaynergyTek) in air with an ambient temperature of 21°C and a relative humidity of 45%. Next, the sample was annealed at 120°C in a glove box for 5 min, forming a ~80-nm-thick HTL on which a 100-nm-thick Ag electrode was deposited by thermal evaporation at a pressure of ~10^{-6} Torr.

The J-V characteristics of photovoltaic cells were recorded on encapsulated devices using a Keithley 2400 source measurement unit under a simulated AM 1.5 G spectrum with a 150 W solar simulator (SAN-EI XES-40S1), and the 100 mW/cm^2 light intensity was calibrated using a pre-calibrated Si-based reference cell with a KG5 filter. EQE spectra of the device were taken using a Enlitech QE-R spectrometer. The film thickness of each layer was determined by a KLA Tencor P-6 profilometer.

Space-Charge-Limited Current Measurements

SCLC measurements were carried out on hole-only and electron-only devices of structure ITO/MoO_3 (10 nm)/blend film/MoO_3 (10 nm)/Al (100 nm) and ITO/ZnO (20 nm)/blend film/LiF (1 nm)/Al (100 nm), respectively. Devices were tested using an Agilent B1500A Semiconductor Parameter Analyzer under ambient. The mobilities were calculated using the following equation to fit the data, and mobilities were calculated from the SCLC region:

$$J = \frac{9}{8}\frac{\varepsilon_r \varepsilon_0 \mu V^2}{d^3}\cdot\exp\left(0.89\gamma\sqrt{\frac{V}{d}}\right), \qquad \text{(Equation 2)}$$

where J is the current density, d is the film thickness, ε_r is the relative dielectric constant of the transport medium, ε_0 is the permittivity of free space (8.85×10^{-12} F m^{-1}), and V is the internal voltage in the device.

Module Fabrication Details

The MoO_3-based modules were fabricated with an architecture similar to that of the MoO_3-based small cells. Patterned ITO glass substrates were cleaned stepwise in detergent, water, acetone, and 2-propanol under ultrasonic irradiation for 10 min and subsequently dried in the oven at 60°C. The ZnO precursor was spin coated onto the patterned ITO substrates and then baked at 120°C for 15 min in air. The TPD-3F (M_n 51 kDa):IT-4F BHJ layer was spin coated or blade coated from *o*-xylene solutions and processed in the air (21°C, with a relative humidity of 45%). When spin coating is used (1,500 rpm, time ~ 60 s), the active layer film is ~100 nm thick and is annealed at 120°C for 5 min under N_2. When blade coating is used, the film is blade coated on a heated substrate (77°C) with a coating velocity of 0.5 m/min and a gap height of 100 μm in the air (21°C, with a relative humidity of 45%) to form a ~145-nm-thick active layer and then annealed at 120°C for 5 min under N_2. For the series connections in the module, the blanket-coated ETL and BHJ layers were patterned by scraping to expose the ITO surface. Next, 8-nm-thick MoO_3 layers and 100-nm-thick Ag electrodes were deposited by thermal evaporation and shadow masking to complete the module and make the Ag to ITO interconnection between adjacent cells. The active area of the module was defined by the shadow mask and the aperture mask as 20.4 cm^2 (4.08 cm^2 for each sub-cell). Finally, the module was encapsulated by cavity glass and sealed with a UV-curable adhesive. The modules incorporating PEDOT:PSS as the HTL were fabricated as indicated above, except the PEDOT:PSS HTL was deposited by blade coating in air (T = 21°C, relative humidity = 45%) a PEDOT:PSS solution (m-PEDOT:PSS from RaynergyTek) on a heated substrate (80°C) with a coating velocity of 0.4 m/min and a gap height of 100 μm. Next, the samples were annealed at 120°C in a glove box for 5 min, forming a ~200-nm-thick HTL on which a 100-nm-thick Ag electrode was deposited by thermal evaporation (pressure = 10^{-6} Torr).

Module Characterization Details

J-V characteristics of photovoltaic module were acquired using a Keithley 2400 source meter under a simulated AM 1.5 G spectrum with a 1,000 W solar simulator (Yamashita Denso YSS-210S), and the 100 mW/cm^2 light intensity was also calibrated using a pre-calibrated Si-based reference cell. To monitor the shelf-life stability of the OPV modules, the encapsulated modules were stored in the dark at 21°C–25°C. The J-V characteristics of the module were measured under AM 1.5 G solar irradiation with a 100 mW/cm^2 light intensity. The light-soaking test was conducted under an alternative metal halide lamp (InfinityPV ISOSun solar simulator). The well-encapsulated and UV-cut-filter-covered devices were maintained at open circuit and light soaked under a 100 mW/cm^2 irradiation with an effectively illuminated area of 30 cm by 30 cm at 55°C for lifetime monitoring. The 100 mW/cm^2 light intensity was calibrated by a Si-based reference cell. The mismatch factor of the solar spectrum was not considered here. The device characteristics were recorded using a Keithley 2400 source measurement unit. For simulated indoor measurements, the J-V characteristics were recorded under a TL84 fluorescent light with a 1,000 lux illumination. The input power of the 1,000 lux

fluorescent lamps was determined using both a Lux meter (TES-1332A) and a StellarNet BLUE-Wave Spectrometer. Before measuring the light intensity at 1,000 lux, the signal in the dark was recorded as the background. The dark spectrum was used to compensate for the instrument noise and dark current thermal drift. The light intensity at 1,000 lux was then calibrated with the dark signal. For indoor lighting, the Lux meter and spectrometer used the following standards as calibration reference standards: CIE S063/CIE S023/ISO 19476/SEMI PV80.

SUPPLEMENTAL INFORMATION

Supplemental Information can be found online at https://doi.org/10.1016/j.joule.2019.11.006.

ACKNOWLEDGMENTS

This work was supported in part by the A+ project of the Ministry of Economic Affairs, Taiwan; the Center for Light Energy Activated Redox Processes (LEAP), an Energy Frontier Research Center funded by the US Department of Energy (DOE), Office of Science, Office of Basic Energy Sciences under award DE-SC0001059 (R.M.Y., M.R.W., and T.J.M.); AFOSR grant FA9550-18-1-0320 (A.F. and Y.C.); the Northwestern University Materials Research Science and Engineering Center under National Science Foundation (NSF) grant DMR-1720139 (B.W. and G.W.); the Flexterra Corporation; and the Institute for Sustainability and Energy at Northwestern (ISEN). Use of the Advanced Photon Source, an Office of Science User Facility operated by the US DOE Office of Science by Argonne National Laboratory, was supported by the US DOE under contract DE-AC02-06CH11357.

AUTHOR CONTRIBUTIONS

C.Y.L., P.H.-S.T., and Y.-M.C. conceived the idea. C.Y.L. designed the synthetic route of the polymers. C.Y.L., C.-H. Lee, and W.-L.L. synthesized the molecules and carried out the characterization. C.-H. Lee also synthesized the small molecular acceptor. The device and module-related design, processes, and characterization were supervised by Y.-M.C.; C.-C.L., N.-W.T., Y.-K.C., C.-H. Li, and H.-L.H. fabricated the devices under different conditions (coating method, processing atmosphere, molecular weight, solvent effect); C.-C.L. fabricated the modules and carried out the characterization. B.W. carried out TEM analysis. A.F. and T.J.M. supervised polymer film and blend characterization. Y.C. performed the SCLC, AFM, TGA, and DSC measurements and G.W. carried out GIWAXS analysis. Y.-C.H. collected the low light performance of devices. R.M.Y. and M.R.W. performed the transient absorption spectroscopy and analysis. Y.-M.C. and A.F. wrote the original version of the manuscript, and all authors discussed the results and contributed to the final production of the manuscript.

DECLARATION OF INTERESTS

Raynergy Tek Incorporation develops and sells organic semiconductors. However, C.-Y.L., C.-C.L., N.-W.T., C.-H. Lee, W.-L.L., Y.-K.C., C.-H. Li, H.-L.H., P.H.-S.T., and Y.-M.C. will not receive any compensation or advancement in career as outcomes of this publication.

Received: August 16, 2019
Revised: October 10, 2019
Accepted: November 1, 2019
Published: December 4, 2019

REFERENCES

1. Du, X., Heumueller, T., Gruber, W., Classen, A., Unruh, T., Li, N., and Brabec, C.J. (2019). Efficient polymer solar cells based on non-fullerene acceptors with potential device lifetime approaching 10 years. Joule *3*, 215–226.

2. Chen, H., Hu, Z., Wang, H., Liu, L., Chao, P., Qu, J., Chen, W., Liu, A., and He, F. (2018). A chlorinated π-conjugated polymer donor for efficient organic solar cells. Joule *2*, 1623–1634.

3. Marrocchi, A., Lanari, D., Facchetti, A., and Vaccaro, L. (2012). Poly(3-hexylthiophene): synthetic methodologies and properties in bulk heterojunction solar cells. Energy Environ. Sci. *5*, 8457–8474.

4. Lee, J., Ko, S.-J., Lee, H., Huang, J., Zhu, Z., Seifrid, M., Vollbrecht, J., Brus, V.V., Karki, A., Wang, H., et al. (2019). Side-chain engineering of nonfullerene acceptors for near-infrared organic photodetectors and photovoltaics. ACS Energy Lett. *4*, 1401–1409.

5. Brus, V.V., Lee, J., Luginbuhl, B.R., Ko, S.J., Bazan, G.C., and Nguyen, T.Q. (2019). Solution-processed semitransparent organic photovoltaics: from molecular design to device performance. Adv. Mater. *31*, 1900904.

6. Li, S., Ye, L., Zhao, W., Yan, H., Yang, B., Liu, D., Li, W., Ade, H., and Hou, J. (2018). A wide band gap polymer with a deep highest occupied molecular orbital level enables 14.2% efficiency in polymer solar cells. J. Am. Chem. Soc. *140*, 7159–7167.

7. Cui, Y., Yao, H., Hong, L., Zhang, T., Xu, Y., Xian, K., Gao, B., Qin, J., Zhang, J., Wei, Z., et al. (2019). Achieving over 15% efficiency in organic photovoltaic cells via copolymer design. Adv. Mater. *31*, e1808356.

8. Song, X., Gasparini, N., Nahid, M.M., Paleti, S.H.K., Wang, J.-L., Ade, H., and Baran, D. (2019). Dual sensitizer and processing-aid behavior of donor enables efficient ternary organic solar cells. Joule *3*, 846–857.

9. Wang, Y., Yan, Z., Guo, H., Uddin, M.A., Ling, S., Zhou, X., Su, H., Dai, J., Woo, H.Y., and Guo, X. (2017). Effects of bithiophene imide fusion on the device performance of organic thin-film transistors and all-polymer solar cells. Angew. Chem. Int. Ed. Engl. *56*, 15304–15308.

10. Zhao, Q.Q., Xiao, Z., Qu, J., Liu, L., Richter, H., Chen, W., Han, L., Wang, M., Zheng, J., Xie, Z., et al. (2019). Elevated stability and efficiency of solar cells via ordered alloy co-acceptors. ACS Energy Lett. *4*, 1106–1114.

11. Baran, D., Ashraf, R.S., Hanifi, D.A., Abdelsamie, M., Gasparini, N., Röhr, J.A., Holliday, S., Wadsworth, A., Lockett, S., Neophytou, M., et al. (2017). Reducing the efficiency-stability-cost gap of organic photovoltaics with highly efficient and stable small molecule acceptor ternary solar cells. Nat. Mater. *16*, 363–369.

12. Ro, H.W., Downing, J.M., Engmann, S., Herzing, A.A., DeLongchamp, D.M., Richter, L.J., Mukherjee, S., Ade, H., Abdelsamie, M., Jagadamma, L.K., et al. (2016). Morphology changes upon scaling a high-efficiency, solution-processed solar cell. Energy Environ. Sci. *9*, 2835–2846.

13. Yu, R., Yao, H., Cui, Y., Hong, L., He, C., and Hou, J. (2019). Improved charge transport and reduced nonradiative energy loss enable over 16% efficiency in ternary polymer solar cells. Adv. Mater. *31*, 1902302.

14. Meng, L., Zhang, Y., Wan, X., Li, C., Zhang, X., Wang, Y., Ke, X., Xiao, Z., Ding, L., Xia, R., et al. (2018). Organic and solution-processed tandem solar cells with 17.3% efficiency. Science *361*, 1094–1098.

15. Liu, X., Du, X., Wang, J., Duan, C., Tang, X., Heumueller, T., Liu, G., Li, Y., Wang, Z., Wang, J., et al. (2018). Efficient organic solar cells with extremely high open-circuit voltages and low voltage losses by suppressing nonradiative recombination losses. Adv. Energy Mater. *8*, 1801699.

16. Xie, Y., Yang, F., Li, Y., Uddin, M.A., Bi, P., Fan, B., Cai, Y., Hao, X., Woo, H.Y., Li, W., et al. (2018). Morphology control enables efficient ternary organic solar cells. Adv. Mater. *30*, 1803045.

17. Zhang, K., Xia, R., Fan, B., Liu, X., Wang, Z., Dong, S., Yip, H.L., Ying, L., Huang, F., and Cao, Y. (2018). .11.2% All-polymer tandem solar cells with simultaneously improved efficiency and stability. Adv. Mater. *30*, 1803166.

18. Xie, C., Heumüller, T., Gruber, W., Tang, X., Classen, A., Schuldes, I., Bidwell, M., Späth, A., Fink, R.H., Unruh, T., et al. (2018). Overcoming efficiency and stability limits in water-processing nanoparticular organic photovoltaics by minimizing microstructure defects. Nat. Commun. *9*, 5335.

19. Mo, D., Wang, H., Chen, H., Qu, S., Chao, P., Yang, Z., Tian, L., Su, Y.-A., Gao, Y., Yang, B., et al. (2017). Chlorination of low-band-gap polymers: toward high-performance polymer solar cells. Chem. Mater. *29*, 2819–2830.

20. Marrocchi, A., Facchetti, A., Lanari, D., Santoro, S., and Vaccaro, L. (2016). Click-chemistry approaches to π-conjugated polymers for organic electronics applications. Chem. Sci. *7*, 6298–6308.

21. Chen, Y., Ye, P., Zhu, Z.G., Wang, X., Yang, L., Xu, X., Wu, X., Dong, T., Zhang, H., Hou, J., et al. (2017). Achieving high-performance ternary organic solar cells through tuning acceptor alloy. Adv. Mater. *29*, 1603154.

22. Xu, X., Feng, K., Bi, Z., Ma, W., Zhang, G., and Peng, Q. (2019). Single-junction polymer solar cells with 16.35% efficiency enabled by a platinum(II) complexation strategy. Adv. Mater. *31*, 1901872.

23. Yuan, J., Zhang, Y., Zhou, L., Zhang, G., Yip, H.-L., Lau, T.-K., Lu, X., Zhu, C., Peng, H., Johnson, P.A., et al. (2019). Single-junction organic solar cell with over 15% efficiency using fused-ring acceptor with electron-deficient core. Joule *3*, 1140–1151.

24. Cui, Y., Yao, H., Zhang, J., Zhang, T., Wang, Y., Hong, L., Xian, K., Xu, B., Zhang, S., Peng, J., et al. (2019). Over 16% efficiency organic photovoltaic cells enabled by a chlorinated acceptor with increased open-circuit voltages. Nat. Commun. *10*, 2515.

25. Yuan, J., Zhang, Y., Zhou, L., Zhang, C., Lau, T.-K., Zhang, G., Lu, X., Yip, H.-L., So, S.K., Beaupré, S., et al. (2019). Fused benzothiadiazole: a building block for n-type organic acceptor to achieve high-performance organic solar cells. Adv. Mater. *31*, 1807577.

26. Yu, R., Yao, H., Chen, Z., Xin, J., Hong, L., Xu, Y., Zu, Y., Ma, W., and Hou, J. (2019). Enhanced π-π interactions of nonfullerene acceptors by volatilizable solid additives in efficient polymer solar cells. Adv. Mater. *31*, 1900477.

27. Lungenschmied, C., Dennler, G., Neugebauer, H., Sariciftci, S.N., Glatthaar, M., Meyer, T., and Meyer, A. (2007). Flexible, long-lived, large-area, organic solar cells. Sol. Energy Mater. Sol. Cells *91*, 379–384.

28. Servaites, J.D., Yeganeh, S., Marks, T.J., and Ratner, M.A. (2010). Efficiency enhancement in organic photovoltaic cells: consequences of optimizing series resistance. Adv. Funct. Mater. *20*, 97–104.

29. Sun, H., Tang, Y., Koh, C.W., Ling, S., Wang, R., Yang, K., Yu, J., Shi, Y., Wang, Y., Woo, H.Y., et al. (2019). High-performance all-polymer solar cells enabled by an n-type polymer based on a fluorinated imide-functionalized arene. Adv. Mater. *31*, e1807220.

30. Hong, S., Kang, H., Kim, G., Lee, S., Kim, S., Lee, J.-H., Lee, J., Yi, M., Kim, J., Back, H., et al. (2016). A series connection architecture for large-area organic photovoltaic modules with a 7.5% module efficiency. Nat. Commun. *7*, 10279.

31. Zhang, T., Zeng, G., Ye, F., Zhao, X., and Yang, X. (2018). Efficient non-fullerene organic photovoltaic modules incorporating as-cast and thickness-insensitive photoactive layers. Adv. Energy Mater. *8*, 1801387.

32. Mori, S., Oh-oka, H., Nakao, H., Gotanda, T., Nakano, Y., Jung, H., Iida, A., Hayase, R., Shida, N., Saito, M., et al. (2015). Organic photovoltaic module development with inverted device structure. MRS Proc. *1737*.

33. Hadmojo, W.T., Wibowo, F.T.A., Ryu, D.Y., Jung, I.H., and Jang, S.Y. (2017). Fullerene-free organic solar cells with an efficiency of 10.2% and an energy loss of 0.59 eV based on a thieno[3,4-c]pyrrole-4,6-dione-containing wide band gap polymer donor. ACS Appl. Mater. Interfaces *9*, 32939–32945.

34. Green, M.A., Hishikawa, Y., Dunlop, E.D., Levi, D.H., Hohl-Ebinger, J., Yoshita, M., and Ho-Baillie, A.W.Y. (2019). Solar cell efficiency tables (version 53). Prog. Photovoltaics *27*, 3–12.

35. Guo, X., Ortiz, R.P., Zheng, Y., Kim, M.G., Zhang, S., Hu, Y., Lu, G., Facchetti, A., and Marks, T.J. (2011). Thieno[3,4-c]pyrrole-4,6-dione-based polymer semiconductors: toward high-performance, air-stable organic thin-film transistors. J. Am. Chem. Soc. *133*, 13685–13697.

36. Yang, Y.Q., Park, H., Lee, S.-H., Kim, D.H., and Lee, Y.-S. (2013). Synthesis of alternating copolymers consisting of *N*-2-octyldodecyldithieno[2,3-b;7,6-b]carbazole and *N*-octylthieno[3,4-c]pyrrole-4,6-dione derivative units for photovoltaic applications. Synth. Met. *176*, 70–77.

37. Zhang, C.-H., Wang, W., Huang, W., Wang, J., Hu, Z., Lin, Z., Yang, T., Lin, F., Xing, Y., Bai, J., et al. (2019). Methyl thioether functionalization of a polymeric donor for efficient solar cells processed from non-halogenated solvents. Chem. Mater. *31*, 3025–3033.

38. Menke, S.M., Ran, N.A., Bazan, G.C., and Friend, R.H. (2018). Understanding energy loss in organic solar cells: toward a new efficiency regime. Joule *2*, 25–35.

39. Eastham, N.D., Logsdon, J.L., Manley, E.F., Aldrich, T.J., Leonardi, M.J., Wang, G., Powers-Riggs, N.E., Young, R.M., Chen, L.X., Wasielewski, M.R., et al. (2018). Hole-transfer dependence on blend morphology and energy level alignment in polymer: ITIC photovoltaic materials. Adv. Mater. *30*, 1704263.

40. Li, Z., Ying, L., Zhu, P., Zhong, W., Li, N., Liu, F., Huang, F., and Cao, Y. (2019). A generic green solvent concept boosting the power conversion efficiency of all-polymer solar cells to 11%. Energy Environ. Sci. *12*, 157–163.

41. Berny, S., Blouin, N., Distler, A., Egelhaaf, H.-J., Krompiec, M., Lohr, A., Lozman, O.R., Morse, G.E., Nanson, L., Pron, A., et al. (2016). Solar trees: first large-scale demonstration of fully solution coated, semitransparent, flexible organic photovoltaic modules. Adv. Sci. *3*, 1500342.

42. Wang, G., Melkonyan, F.S., Facchetti, A., and Marks, T.J. (2019). All-polymer solar cells: recent progress, challenges, and prospects. Angew. Chem. Int. Ed. Engl. *58*, 4129–4142.

43. Wang, G., Swick, S.M., Matta, M., Mukherjee, S., Strzalka, J.W., Logsdon, J.L., Fabiano, S., Huang, W., Aldrich, T.J., Yang, T., et al. (2019). Photovoltaic blend microstructure for high efficiency post-fullerene solar cells. To tilt or not to tilt? J. Am. Chem. Soc. *141*, 13410–13420.

44. Zhou, N., Dudnik, A.S., Li, T.I., Manley, E.F., Aldrich, T.J., Guo, P., Liao, H.-C., Chen, Z., Chen, L.X., Chang, R.P., et al. (2016). All-polymer solar cell performance optimized via systematic molecular weight tuning of both donor and acceptor polymers. J. Am. Chem. Soc. *138*, 1240–1251.

45. Deshmukh, K.D., Matsidik, R., Prasad, S.K.K., Connal, L.A., Liu, A.C.Y., Gann, E., Thomsen, L., Hodgkiss, J.M., Sommer, M., and McNeill, C.R. (2018). Tuning the molecular weight of the electron accepting polymer in all-polymer solar cells: impact on morphology and charge generation. Adv. Funct. Mater. *28*, 1707185.

46. Li, S., Ye, L., Zhao, W., Liu, X., Zhu, J., Ade, H., and Hou, J. (2017). Design of a new small-molecule electron acceptor enables efficient polymer solar cells with high fill factor. Adv. Mater. *29*, 1704051.

47. Aldrich, T.J., Matta, M., Zhu, W., Swick, S.M., Stern, C.L., Schatz, G.C., Facchetti, A., Melkonyan, F.S., and Marks, T.J. (2019). Fluorination effects on indacenodithienothiophene acceptor packing and electronic structure, end-group redistribution, and solar cell photovoltaic response. J. Am. Chem. Soc. *141*, 3274–3287.

48. Lucera, L., Machui, F., Kubis, P., Schmidt, H.D., Adams, J., Strohm, S., Ahmad, T., Forberich, K., Egelhaaf, H.-J., and Brabec, C.J. (2016). Highly efficient, large area, roll coated flexible and rigid OPV modules with geometric fill factors up to 98.5% processed with commercially available materials. Energy Environ. Sci. *9*, 89–94.

49. Cutting, C.L., Bag, M., and Venkataraman, D. (2016). Indoor light recycling: a new home for organic photovoltaics. J. Mater. Chem. C *4*, 10367–10370.

50. Zhao, W., Li, S., Yao, H., Zhang, S., Zhang, Y., Yang, B., and Hou, J. (2017). Molecular optimization enables over 13% efficiency in organic solar cells. J. Am. Chem. Soc. *139*, 7148–7151.

51. Young, R.M., Dyar, S.M., Barnes, J.C., Juríček, M., Stoddart, J.F., Co, D.T., and Wasielewski, M.R. (2013). Ultrafast conformational dynamics of electron transfer in $ExBox^{4+} \subset$ perylene. J. Phys. Chem. A *117*, 12438–12448.